



Novel Catalyst Composites of Ni-and Co-Based Nanoparticles Supported on Inorganic Oxides for Fatty Acid Hydrogenations

Ekaterina Mamontova, Corine Trabbia, Isabelle Favier, Alejandro Serrano-Maldona, Jean-Bernard Ledeuil, L  na  c Madec, Montserrat G  mez, Daniel Pla

► To cite this version:

Ekaterina Mamontova, Corine Trabbia, Isabelle Favier, Alejandro Serrano-Maldona, Jean-Bernard Ledeuil, et al.. Novel Catalyst Composites of Ni-and Co-Based Nanoparticles Supported on Inorganic Oxides for Fatty Acid Hydrogenations. *Nanomaterials*, 2023, 13, pp.1435. <10.3390/nano13091435>. <hal-04079541>

HAL Id: hal-04079541

<https://hal.science/hal-04079541v1>

Submitted on 24 Apr 2023

HAL is a multi-disciplinary open access archive for the deposit and dissemination of scientific research documents, whether they are published or not. The documents may come from teaching and research institutions in France or abroad, or from public or private research centers.

L'archive ouverte pluridisciplinaire **HAL**, est destin  e au d  p  t et    la diffusion de documents scientifiques de niveau recherche, publi  s ou non,   manant des   tablissements d'enseignement et de recherche fran  ais ou   trangers, des laboratoires publics ou priv  s.



HAL Authorization



Article

Novel Catalyst Composites of Ni- and Co-Based Nanoparticles Supported on Inorganic Oxides for Fatty Acid Hydrogenations

Ekaterina Mamontova ¹, Corine Trabbia ¹, Isabelle Favier ¹, Alejandro Serrano-Maldonado ¹, Jean-Bernard Ledeuil ², L  na  c Madec ², Montserrat G  mez ^{1,*} and Daniel Pla ^{1,*}

- ¹ Laboratoire H  t  rochimie Fondamentale et Appliqu  e, UMR CNRS 5069, Universit   Toulouse III—Paul Sabatier, 118 Route de Narbonne, CEDEX 9, 31062 Toulouse, France; ekaterina.mamontova@umontpellier.fr (E.M.); corine.trabbia@gmail.com (C.T.); isabelle.favier@univ-tlse3.fr (I.F.); alejandro.serrano@univ-tlse3.fr (A.S.-M.)
- ² E2S UPPA, CNRS, IPREM, Universit   de Pau et des Pays de l'Adour, 64053 Pau, France; jledeuil@univ-pau.fr (J.-B.L.); lena  c.madec@univ-pau.fr (L.M.)
- * Correspondence: montserrat.gomez-simon@univ-tlse3.fr (M.G.); pla@lhfa.fr (D.P.)

Abstract: In the quest to develop nanometrically defined catalytic systems for applications in the catalytic valorization of agri-food wastes, small Ni-based nanoparticles supported on inorganic solid supports have been prepared by decomposition of organometallic precursors in refluxing ethanol under H₂ atmosphere, in the presence of supports exhibiting insulating or semi-conductor properties, such as MgAl₂O₄ and TiO₂, respectively. The efficiency of the as-prepared Ni-based nanocomposites has been evaluated towards the hydrogenation of unsaturated fatty acids under solvent-free conditions, with high selectivity regarding the hydrogenation of C=C bonds. The influence of the support on the catalytic performance of the prepared Ni-based nanocomposites is particularly highlighted.



Citation: Mamontova, E.; Trabbia, C.; Favier, I.; Serrano-Maldonado, A.; Ledeuil, J.-B.; Madec, L.; G  mez, M.; Pla, D. Novel Catalyst Composites of Ni- and Co-Based Nanoparticles Supported on Inorganic Oxides for Fatty Acid Hydrogenations. *Nanomaterials* **2023**, *13*, 1435. <https://doi.org/10.3390/nano13091435>

Academic Editors: Dominique Agustin, Jana Pisk and Ioannis V. Yentekakis

Received: 3 April 2023
Revised: 17 April 2023
Accepted: 19 April 2023
Published: 22 April 2023



Copyright:    2023 by the authors. Licensee MDPI, Basel, Switzerland. This article is an open access article distributed under the terms and conditions of the Creative Commons Attribution (CC BY) license (<https://creativecommons.org/licenses/by/4.0/>).

Keywords: nickel-based nanoparticles; magnesium aluminum oxide spinel; titanium dioxide anatase; C=C bonds hydrogenation; fatty acids; valorization; industrial waste

1. Introduction

Despite the fact that the valorization of fatty wastes in the form of fatty esters has long been studied, the corrosive nature of fatty acids makes their transformation into free acid form a more challenging quest in terms of scaling up or intensification for industrial applications provided that robust catalyst solutions withstanding the reaction conditions are found. Since the seminal works of Paul Sabatier regarding nickel reactivity [1,2] and its further applications in catalytic hydrogenations [3,4], the quest for attaining high activity and selectivity while overriding deleterious catalyst passivation pathways has resulted in a number of preparations, with the aim of preserving the catalyst dispersion due to its key implications towards reactivity [5]. Raney nickel was described for the first time in 1925 [6] and Raney cobalt in 1933 [7]; intermetallic nickel–aluminum and cobalt–aluminum alloys, respectively, featuring mesoporous structures upon activation via alkaline treatment, have been widely used as hydrogenation catalysts [5,8], such as for the industrial production of hexamethylenediamine from adiponitrile [9] and margarine both from vegetable oils and animal fats [10]. In particular, the correlation between Raney nickel catalyst microstructure (NiAl₃ vs. Ni₂Al₃) and catalytic performance has been recently established [11], providing new means towards rational catalyst design involving inorganic supports. Later on, Ni-based Urushibara [12] and Kieselguhr hydrogenation catalysts [13,14], as well as cobalt-based ones [15–17], have also been reported in the literature, affording new means to attain zero-valent nickel and cobalt phases that play essential roles in catalytic C=C bond hydrogenation reactions. To reduce Ni soap formation,

fatty acid hydrogenations are generally carried out at high pressures (20–30 bar) and temperatures in the range of 180–210 °C with pre-dried samples [18].

A particular type of composite materials made of Al_2O_3 –Ni and Al_2O_3 –NiO with a spinel-phase NiAl_2O_4 [19] have been used as (pre)catalysts for reforming reactions due to their high thermal stability [20,21]. Many preparative protocols under a sintering atmosphere [13–16] have been described (namely, powder coating [22], sol–gel [23], hydrothermal and solvothermal methods [10], and impregnation [12]), triggering in some cases the structural transformation of NiAl_2O_4 from normal spinel (Ni^{2+})[Al_2^{3+}] O_4 to an inverse one, (Al^{3+})[$\text{Ni}^{2+}\text{Al}^{3+}$] O_4 [24]. The corrosion constraints associated with the hydrogenation of fatty acids and potential catalyst deactivation pathways poised us to select neutral metal oxide supports with enhanced thermal stability and mechanical robustness, such as titanium dioxide (TiO_2) and magnesium aluminum oxide spinel (MgAl_2O_4) owing to their relatively high activity in hydrogenations and reforming processes [25–28], low cost, and wide availability.

Nanocatalysis provides innovative solutions towards catalyst enhancements via kinetic stabilization at the nanoscale of small particles, thus providing high surface-metal ratios together with a number of highly reactive metal sites arising from low-coordination defects, as well synergistic effects at the metal-support interfaces for heterogeneized systems [29]. Based on our previous experience [30,31], herein we describe the synthesis of original mono-metallic and bi-metallic Ni and/or Co-based nanocomposites by a one-step methodology, resulting in well-defined metal nanoparticles (MNPs) supported on TiO_2 or MgAl_2O_4 . Working under smooth conditions, this approach permits a straightforward MNPs incorporation on the support surface, as well as overriding potential structural changes of the supports. These as-prepared catalytic materials exhibited remarkable activity in the hydrogenation processes of fatty acids, including their application in waste valorization.

2. Materials and Methods

2.1. Materials

All reagents were purchased at the highest commercial quality and used without further purification unless stated otherwise. Halloysite and quinidine were dried in a Schlenk flask under vacuum at 100 °C overnight prior to use. The synthesis of metal nanoparticles was performed in Fisher–Porter bottles. The synthesized catalytic materials were isolated by centrifugation and dried under vacuum at 100 °C overnight; the dried materials were stored in a glove box. Solvents were previously dried on a solvent purifier system and degassed via three freeze-pump-thaw cycles. High-pressure hydrogenation reactions were carried out in stainless steel autoclaves acquired from Parr and Top Industries.

For general experimentation details and characterization techniques, see Supplementary Materials.

2.2. Synthesis of Supported Metal Nanoparticles

2.2.1. Synthesis of Nickel Nanoparticles Stabilized by Quinidine and Supported on MgAl_2O_4 or TiO_2 , $\text{NiNP@MgAl}_2\text{O}_4$, and NiNP@TiO_2 , Respectively

A Fisher–Porter bottle was charged with bis(1,5-cyclooctadiene)nickel(0) (234.3 mg, 0.85 mmol), quinidine (276.4 mg, 0.85 mmol), and the support (1 g of MgAl_2O_4 or TiO_2 -P90) and then sealed with a septum inside the glove box. The Fisher–Porter bottle was then removed from the glove box, and the solid mixture was suspended in degassed EtOH (32 mL) under an argon atmosphere prior to sealing the Fisher–Porter with its head. The system was pressurized with H_2 (3 bar) at room temperature and then heated up to 100 °C and stirred for 18 h. A black dispersion was obtained and transferred to a centrifuge tube via cannulation under Ar. Centrifugation was carried out at 3500 rpm for 10 min. After removing the supernatant, the solid was dispersed in degassed EtOH (rinsing repeated three times). The obtained black solid was dried under a vacuum overnight and stored in the glove box prior to use. $\text{NiNP@MgAl}_2\text{O}_4$: 750 mg (72% yield); NiNP@TiO_2 : 1000 mg (95% yield).

2.2.2. Synthesis of Cobalt Nanoparticles Stabilized by Quinidine and Supported on MgAl_2O_4 and TiO_2 , $\text{CoNP@MgAl}_2\text{O}_4$, and CoNP@TiO_2

A Fisher–Porter bottle was charged with dicobalt octacarbonyl (145.1 mg, 0.42 mmol), quinidine (275.1 mg, 0.85 mmol), and the support (1 g of MgAl_2O_4 or TiO_2 -P90) and then sealed with a septum inside the glove box. The Fisher–Porter bottle was then removed from the glove box, and the solids were suspended in degassed EtOH (32 mL) under Ar prior to sealing the Fisher–Porter with its head. The system was pressurized with H_2 (3 bar) at room temperature and then heated to 100 °C and stirred for 18 h. A black dispersion was obtained and transferred to a centrifuge tube via cannulation under Ar. Centrifugation was carried out at 3500 rpm for 10 min. After the removal of the supernatant, the solid was dispersed in degassed EtOH (rinsing repeated three times). The obtained black solid was dried under a vacuum overnight and stored in the glove box prior to use. **CoNP@MgAl₂O₄**: 570 mg (54% yield); **CoNP@TiO₂**: 993 mg (94% yield).

2.2.3. Synthesis of Nickel–Cobalt Nanoparticles Stabilized by Quinidine and Supported on MgAl_2O_4 or TiO_2 , $\text{NiCoNP@MgAl}_2\text{O}_4$, and NiCoNP@TiO_2 , Respectively

A Fisher–Porter bottle was charged with dicobalt octacarbonyl (36.9 mg, 0.11 mmol), bis(1,5-cyclooctadiene)nickel(0) (59.1 mg, 0.22 mmol), quinidine (139.4 mg, 0.42 mmol), and the support (500 mg of MgAl_2O_4 or TiO_2 -P90) and then sealed with a septum inside the glove box. The Fisher–Porter bottle was then removed from the glove box, and the solid mixture was suspended in degassed EtOH (16 mL) under Ar prior to sealing the Fisher–Porter with its head. The system was pressurized with H_2 (3 bar) at room temperature and then heated to 100 °C and stirred for 18 h. A black dispersion was obtained and transferred to a centrifuge tube via cannulation under Ar. Centrifugation was carried out at 3500 rpm for 10 min. After the removal of the supernatant, the solid was dispersed in degassed EtOH (rinsing repeated three times). The obtained black solid was dried under a vacuum overnight and stored in the glove box prior to use. **NiCoNP@MgAl₂O₄**: 450 mg (84% yield); **NiCoNP@TiO₂**: 520 mg (97% yield).

2.2.4. Extraction of Metal Nanoparticles from the Inorganic Support with Glycerol

For characterization purposes, 70 mg of catalytic material was dispersed in 5 mL of glycerol. The mixture was stirred overnight at room temperature. A black dispersion was obtained and transferred to a centrifuge tube via cannulation under Ar. Centrifugation was carried out at 3500 rpm for 15 min. The obtained glycerol phase was analyzed by TEM to determine average nanoparticle diameters with size distributions.

2.3. Catalytic Hydrogenation Reactions Using $\text{NiNP@MgAl}_2\text{O}_4$

A small glass flask containing 12 mg (0.01 mmol Ni) of nickel nanoparticles **NiNP@MgAl₂O₄** with 285 mg of oleic acid (1 mmol), weighted in a glove box, was introduced in an autoclave under an argon atmosphere. The mixture was then pressurized under 5 bar H_2 and heated at 250 °C with an aluminum heating block for 30 min. At the end of the reaction, the organic products were extracted with dichloromethane (5 × 3 mL), the solution was filtered through a 0.6- μm PTFE syringe filter, and the solvent was evaporated under a vacuum. Conversion and selectivity were determined by ^1H NMR using 4-methylanisole as the internal standard. Reported catalytic results correspond to the mean values obtained for three replicates.

3. Results and Discussion

3.1. Design and Characterization of Nanocomposite Materials

With the aim of efficiently immobilizing mono-metallic Ni- (NiNP), Co- (CoNP), and bi-metallic NiCo nanoparticles (NiCoNP) on inorganic oxides (MgAl_2O_4 and TiO_2), we used herein a methodology based on the decomposition of organometallic precursors, either bis(1,5-cyclooctadiene)nickel(0), octacarbonyldicobalt(0), or a combination of both under H_2 atmosphere (3 bar) in the presence of quinidine as a stabilizer and a suspension of the solid

support in ethanol under stirring at 100 °C overnight, adapting a methodology that has been recently described by our group for the preparation of Ni-based halloysite nanocomposites [31]. Thus, the synthesis of six nanocomposite materials, namely **NiNP@MgAl₂O₄**, **CoNP@MgAl₂O₄**, **NiCoNP@MgAl₂O₄**, **NiNP@TiO₂**, **CoNP@TiO₂**, and **NiCoNP@TiO₂** was achieved (Figure 1). For the bi-metallic systems, a nickel:cobalt ratio of 1:1 was used.

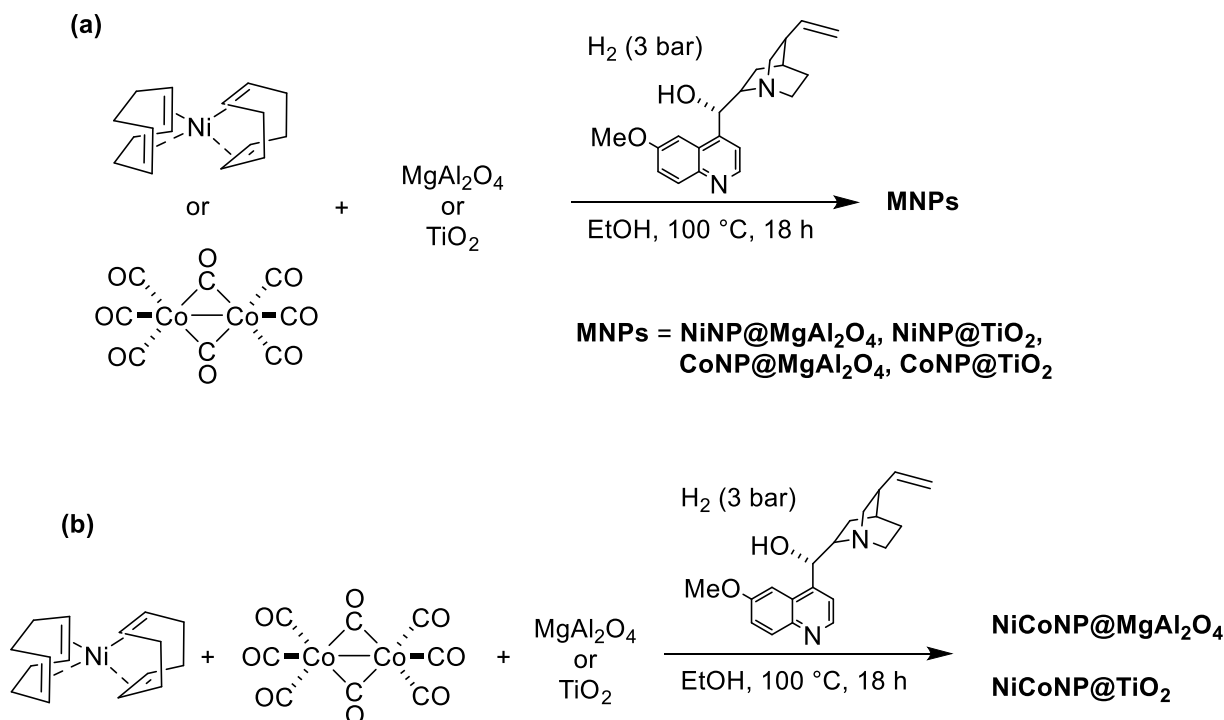


Figure 1. (a) Synthesis of both mono-metallic Ni and Co nanocomposites supported on MgAl₂O₄ or TiO₂; (b) synthesis of bi-metallic NiCo nanocomposites supported on MgAl₂O₄ or TiO₂.

The sizes of metal NPs could not be directly estimated by TEM from the as-prepared composites due to the difficulty of distinguishing the metal NPs from the support; therefore, metal NPs were extracted from the corresponding support with glycerol for characterization purposes taking advantage of the high affinity of MNPs for the glycerol phase [32–35]. As observed by TEM analyses of the glycerol dispersions (direct analyses thanks to the negligible vapor pressure of glycerol), well-dispersed small Ni nanoparticles were obtained from both MgAl₂O₄ and TiO₂ supports (mean diameter: 1.4 ± 0.4 nm and 1.6 ± 0.5 nm for **NiNP@MgAl₂O₄** and **NiNP@TiO₂**, respectively, for 1466 and 2064 particles, respectively; Figure 2), in agreement with our previous contributions involving nickel nanoparticles [30,31]. For the analogous mono-metallic Co systems, well-dispersed small Co nanoparticles were also obtained independently from the support used (mean diameter: 1.2 ± 0.3 nm and 1.3 ± 0.3 nm for **CoNP@MgAl₂O₄** and **CoNP@TiO₂**, respectively, for 1103 and 1493 particles, respectively). Moreover, for the NiCo bi-metallic systems, the glycerol extraction was only efficient for **NiCoNP@TiO₂** (mean diameter: 1.2 ± 0.4 nm for 3868 particles).

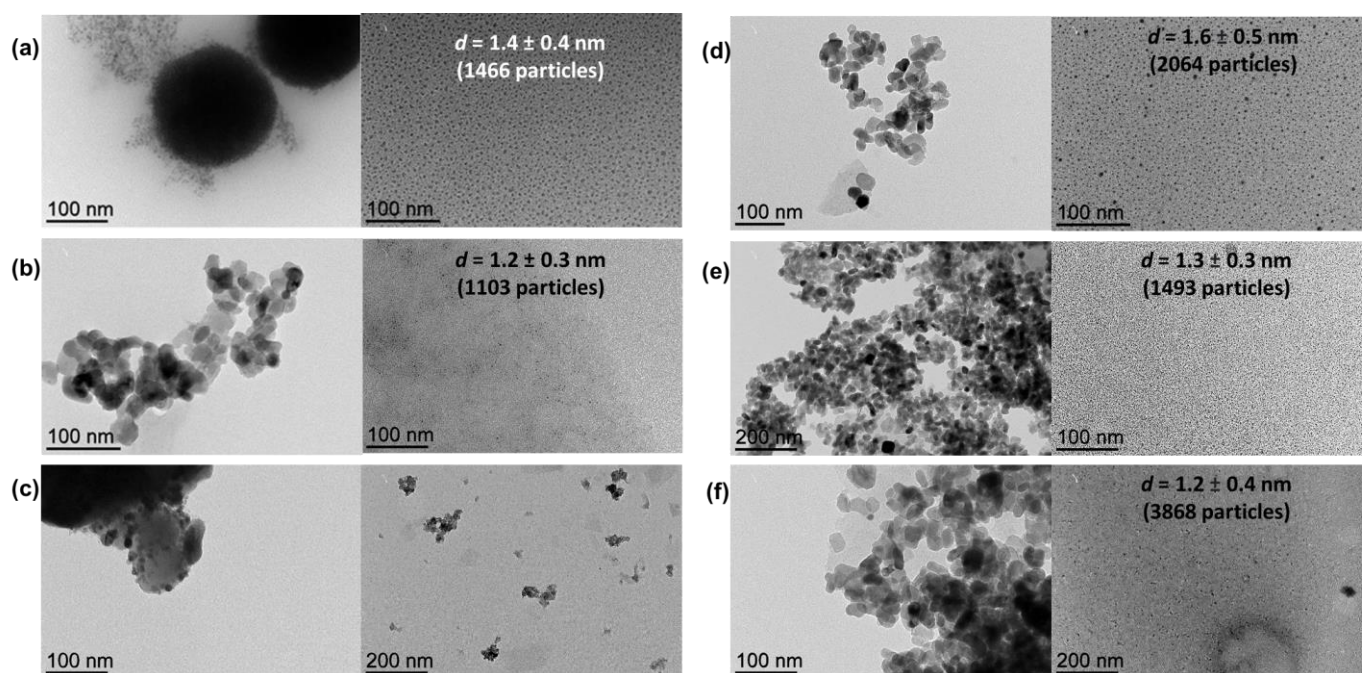


Figure 2. TEM micrographs of nickel-based nanocomposite materials: (a) NiNP@MgAl₂O₄ after synthesis and glycerol extracts with particle size distribution (1.4 ± 0.4 nm for 1466 particles); (b) CoNP@MgAl₂O₄ after synthesis and glycerol extracts with particle size distribution (1.2 ± 0.3 nm for 1103 particles); (c) NiCoNP@MgAl₂O₄ after synthesis and glycerol extracts; (d) NiNP@TiO₂ after synthesis and glycerol extracts with particle size distribution (1.6 ± 0.5 nm for 2046 particles); (e) CoNP@TiO₂ after synthesis and glycerol extracts with particle size distribution (1.3 ± 0.3 nm for 1493 particles); (f) and NiCoNP@TiO₂ after synthesis and glycerol extracts with particle size distribution (1.2 ± 0.4 nm for 3868 particles) (see Figures S1–S6 for further TEM micrographs of each material in the Supplementary Materials).

Scanning Transmission Electron Microscopy Bright Field (STEM-BF), mapping on an HRTEM image corresponding to NiCoNP@TiO₂ evidenced a homogeneous dispersion of nickel and cobalt over the support surface, suggesting an alloy structure (Figure 3 and Figure S7 in the Supplementary Materials for another HRTEM image). However, the small size of the as-prepared nanoparticles lies at the limit of current characterization techniques. It is worth mentioning that the insulating nature of MgAl₂O₄ as support hampered HRTEM analysis due to charging effects observed during acquisition at 200 KV.

ICP-AES analyses of the as-prepared materials were consistent with an efficient metal deposition over both supports: 4.6 wt% Ni for both NiNP@MgAl₂O₄ and NiNP@TiO₂; 4.5 wt% Co for both CoNP@MgAl₂O₄ and CoNP@TiO₂; 3.0 wt% Ni and 1.8 wt% Co for NiCoNP@MgAl₂O₄, as well as 2.8 wt% Ni and 2.6 wt% Co for NiCoNP@TiO₂ (expected data: 5 wt% Ni, 5 wt% Co or overall Ni–Co metal content). In addition, the presence of C and N in the as-prepared materials could be determined by elemental analyses, evidencing the presence of quinidine acting as a stabilizer in the final materials (N content: lower than 0.3 wt% for all composite materials, see Table S1 in the Supplementary Materials for further details). Powder X-ray diffraction analyses of the four nanocomposites only exhibited the corresponding peaks of MgAl₂O₄ and TiO₂ supports; probably, the 5 wt% metal loading (of Ni and/or Co) content falling below the limits of detection for this technique, together with potential peak broadening effects arising from the small size of NiNP and NiCoNP, in particular for NiNP@MgAl₂O₄, NiNP@TiO₂, and NiCoNP@TiO₂ (see Figures S8–S13 in the Supplementary Materials).

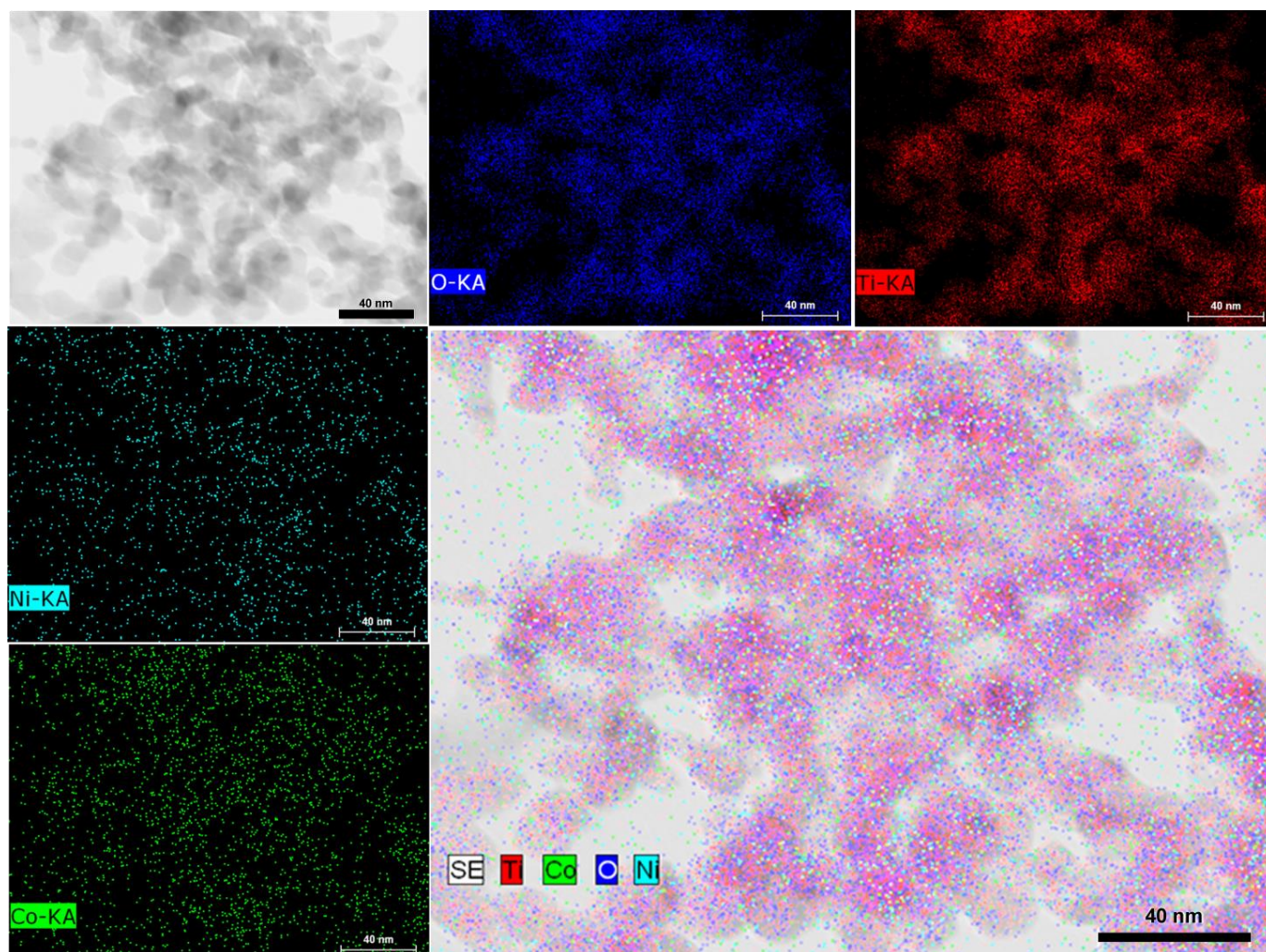


Figure 3. STEM-BF analysis of **NiCoNP@TiO₂** showing elemental distribution of Ti (red), Co (green), Ni (cyan), and O (blue).

With the aim of assessing the presence of quinidine or potential metal oxides on the as-prepared Ni-based materials, diffuse reflectance infrared Fourier transform spectroscopy (DRIFTS) analyses were carried out (Figures S14 and S15 in the Supplementary Materials). For **NiNP@TiO₂**, **CoNP@TiO₂** **NiCoNP@TiO₂** absorption bands corresponding to C–H stretching of quinidine (ca. 3000–2840 cm^{-1}) were identified together with the characteristic bands in the region ca. 1630–1450 cm^{-1} , confirming the presence of quinidine (Figure S14 in the Supplementary Materials). In agreement with the lower quinidine content determined by elemental analysis for **MgAl₂O₄** spinel composites, the qualitative presence of quinidine in **NiNP@MgAl₂O₄**, **CoNP@MgAl₂O₄**, and **NiCoNP@MgAl₂O₄** could not be assessed by DRIFTS (see Figure S15 in the Supplementary Materials). In addition, the intense absorption bands obtained for these composites in the region of 900–450 cm^{-1} corresponding to Al–O and Mg–O bond stretching vibrations of the support, do not permit to exclude the presence of metal oxides (stretching vibrations: 700–600 cm^{-1} for Ni–O and 680–558 cm^{-1} for Co–O) see Figure S15 in the Supplementary Materials).

Moreover, magnetic measurements were carried out for the Ni-based nanocomposites at 2 K (Figure 4, Table 1). Magnetic measurements for the mono-metallic **NiNP@MgAl₂O₄** and **NiNP@TiO₂** systems were carried out, showing a weak ferromagnetic behavior for both materials, with a narrow hysteresis at 2 K with coercive fields of 775 and 947 Oe, respectively, together with moderate remanence magnetization (25.2 and 8.3 emu/gNi , respectively). The saturation magnetization values (M_s) for **NiNP@MgAl₂O₄** (63.7 emu/g)

were similar to those reported for bulk nickel (54 emu/g) [36,37]; however, for NiNP@TiO₂ the M_s (29 emu/g) was lower probably due to either spin capping effects from stabilizers over the surface of nickel nanoparticles or the presence of nickel oxides.

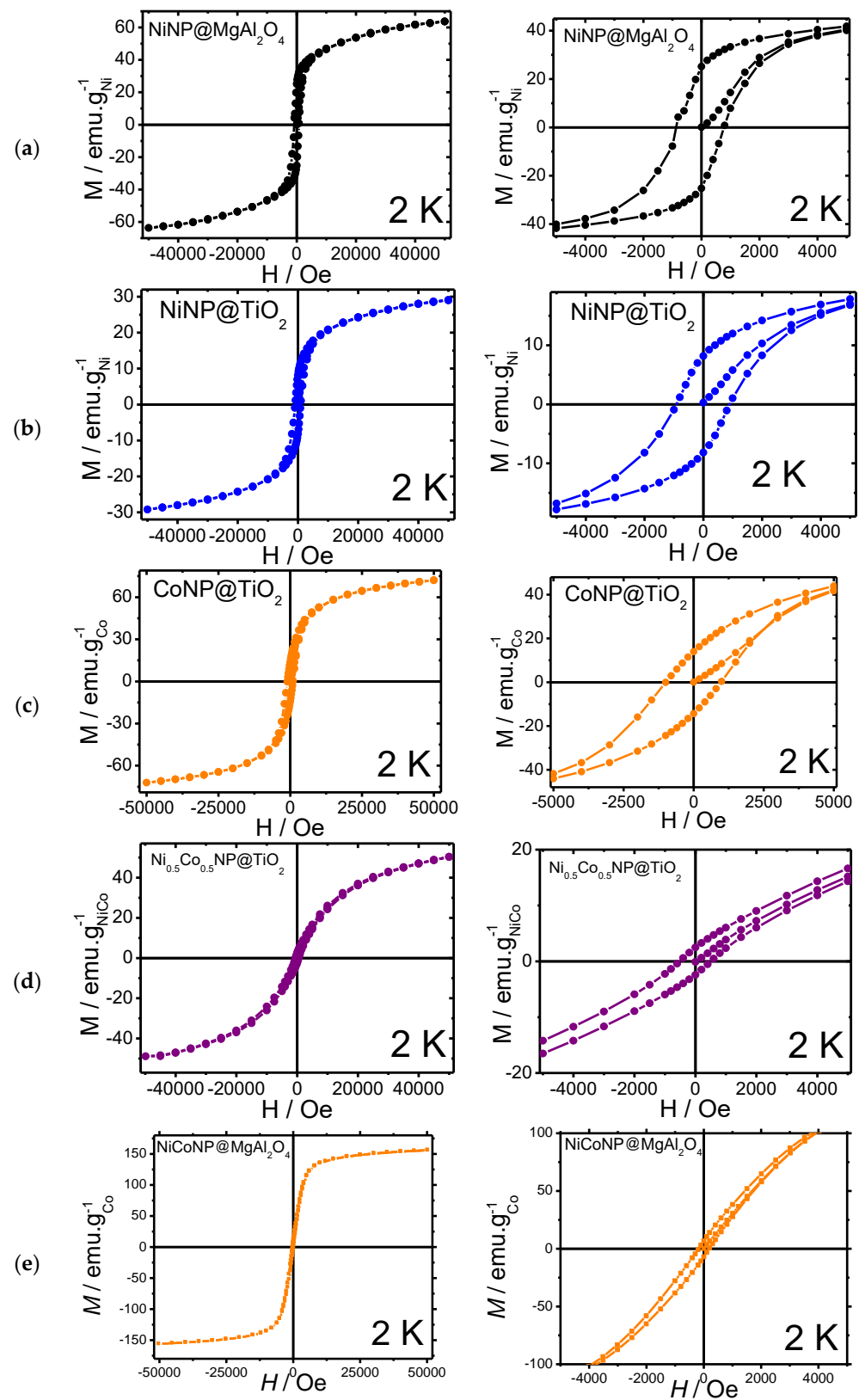


Figure 4. Magnetization curves with magnification: (a) NiNP@MgAl₂O₄; (b) NiNP@TiO₂; (c) CoNP@TiO₂; (d) NiCoNP@TiO₂; (e) NiCoNP@MgAl₂O₄.

Table 1. Magnetic parameters for supported metal NPs.

Sample	H _c (Oe)	M _r ^{MNPs} (emu.g ^{−1})	M _s ^{MNPs} (emu.g ^{−1})
NiNP@MgAl ₂ O ₄	775	25.2	63.7
NiNP@TiO ₂	947	8.3	29.1
CoNP@TiO ₂	982	13.7	72.0
NiCoNP@MgAl ₂ O ₄	181	6.7	156.2
NiCoNP@TiO ₂	511	2.7	52.0

In comparison to the mono-metallic composites, magnetic measurements of the bi-metallic systems **NiCoNP@MgAl₂O₄** and **NiCoNP@TiO₂** showed a superparamagnetic behavior, with narrow hystereses at 2 K and coercive field values of 511 and 181 Oe, respectively, together with the lowest remanence magnetizations (6.7 and 2.7 emu/gNiCo, respectively). Moreover, **NiCoNP@MgAl₂O₄** and **NiCoNP@TiO₂** presented lower M_s values (156.2 and 52.0 emu/gNiCo) than the value for Co-hcp (162 emu/g) [38]. The lower value obtained for **NiCoNP@TiO₂** in comparison to the Ni reference (54 emu/g for bulk Ni) could be due to the presence of nickel and cobalt oxides or the presence of capping agents, such as quinidine [39–42].

Given the fast oxidation of the samples during the introduction to the experimental station, X-ray absorption spectroscopy (XAS) analyses of **NiNP@MgAl₂O₄**, **NiNP@TiO₂**, **NiCoNP@MgAl₂O₄**, and **NiCoNP@TiO₂** could only confirm the presence of nickel and/or cobalt oxides, mainly attributed to NiO or Ni(OH)₂ (Figure S16 in the Supplementary Materials) and CoO (Figure S17 in the Supplementary Materials) [43].

Considering the high catalytic performance of both **NiNP@MgAl₂O₄** and **NiCoNP@MgAl₂O₄** (see below, Section 3.2), further characterization of these composite materials was performed. X-Ray photoelectron spectroscopy (XPS) analyses were carried out to determine the oxidation state of nickel and cobalt species immobilized on MgAl₂O₄, as well as the elements present at the surface of the catalytic materials (Figure 5). The XPS survey spectrum of the MgAl₂O₄ support showed the expected peaks for Mg, Al, and O. The XPS quantification showed that MgAl₂O₄ accounts for about 24 at.% while Al₂O₃ is also present with about 60 at.% in accordance to previous reports concerning solid solutions of Al₂O₃ phases in MgAl₂O₄ closer to the composition of stoichiometric spinel [44]. For **NiNP@MgAl₂O₄**, peaks for Ni were also observed, with a Ni content of 13 at.%. Notably, the Ni 2p XPS core level spectra showed three contributions from Ni metal (18%), NiO (26%), and Ni(OH)₂ (56%). For **NiCo@MgAl₂O₄**, peaks for both Ni and Co were also observed, which account for a low content of about 1 at.% each. Significantly, the Ni 2p XPS core level spectra showed three contributions from Ni metal (17%), NiO (53%), and Ni(OH)₂ (50%), and the Co 2p XPS core level spectra showed three contributions from Co metal (16%), CoO (40%), and Co(OH)₂ (44%) (see Figure S18 and Table S2 in the Supplementary Materials). Despite the fact that Co₃O₄ is thermodynamically more stable than CoO, the coexistence of Co(II) and Co(III) species is difficult to assess given their close binding energies (779.5 and 781.3 eV, respectively) [39–42,45]. However, a better fitting of the Co 2p_{3/2} XPS core level spectra with the envelopes corresponding to Co 2p_{3/2} peaks of the following references Co(0), Co₃O₄, CoO, Co(OH)₂ was obtained with a slight constraint on the position of each, where the presence of Co₃O₄ fell to zero. It is noteworthy to highlight that although Co₃O₄ could only be estimated if CoO was imposed to be zero, Co(0) content was similar for both fittings. Overall, these results highlight that the preparation method for **Ni@MgAl₂O₄** and **NiCo@MgAl₂O₄** is effective in obtaining mono and bi-metallic NPs, albeit with partial oxidation. It is important to mention that due to the rapid oxidation of Ni(0) and Co(0), even under an Ar glove box atmosphere or ultra-high vacuum, XPS analyses of such powder samples were a challenge. Consequently, the real at.% of Ni and Co metal in the samples is probably higher than the values reported herein.

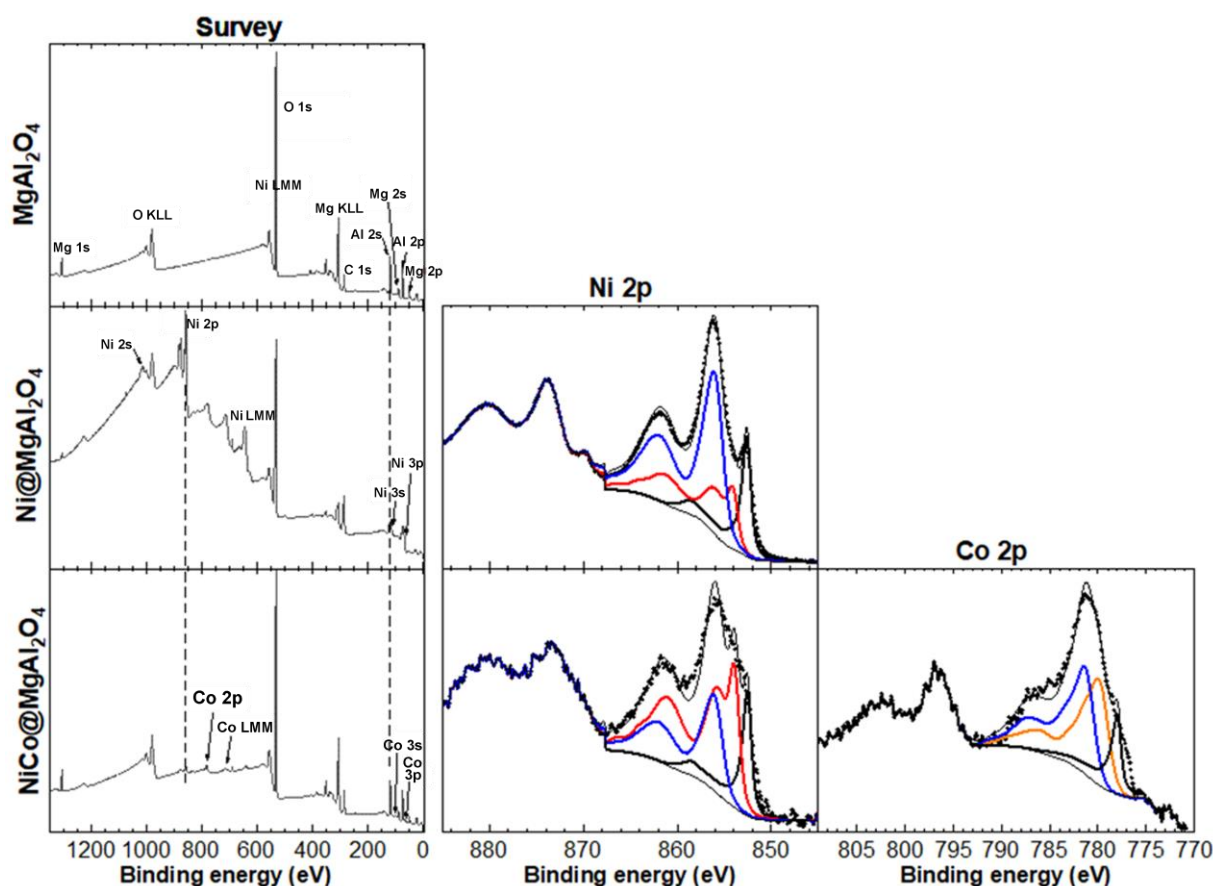


Figure 5. XPS analyses: XPS survey spectra of MgAl_2O_4 support, $\text{NiNP@MgAl}_2\text{O}_4$ and $\text{NiCoNP@MgAl}_2\text{O}_4$ composites (left column); high-resolution spectrum at the binding energy region of Ni 2p; black, red, and blue continuous traces correspond to Ni(0), NiO, and Co(OH)_2 envelopes used to fit the experimental data (dotted line); the fit was carried out on the Ni $2p_{3/2}$ binding energy (middle column); high-resolution spectrum at the binding region of Co 2p; black, orange, and blue continuous traces correspond to Co(0), CoO, and Co(OH)_2 envelopes used to fit the experimental data (dotted line); the fit was carried out on the Co $2p_{3/2}$ binding energy (right column). For the peak fitting procedures, see the experimental section.

3.2. Catalytic Hydrogenation of Fatty Acids

The catalytic behavior of the six as-prepared nanocomposites was assessed in the hydrogenation of oleic acid (**1**) towards stearic acid (**2**) as a benchmark reaction (Table 2). Under neat conditions, working at 180 °C, 5 bar H_2 pressure, and 1 mol% of metal loading (for the bi-metallic catalyst, 0.5 mol% Ni and 0.5 mol% Co), titania nanocomposites CoNP@TiO_2 , NiNP@TiO_2 , and NiCoNP@TiO_2 only gave low to moderate conversions (10%, 65%, and 31% conversions, respectively; entries 1–3, Table 2), highlighting the positive impact of mono-metallic NiNPs in terms of catalyst efficiency (entry 2 vs. 1 and 3, Table 2). In agreement with this trend, the analogous MgAl_2O_4 spinel-based nanocomposite system with CoNPs, $\text{CoNP@MgAl}_2\text{O}_4$, also exhibited a poor performance (12% conversion; entry 4, Table 2). Nevertheless, $\text{NiNP@MgAl}_2\text{O}_4$ and $\text{NiCoNP@MgAl}_2\text{O}_4$ were more active than titania-derived catalytic materials (96 and 93% conversions, respectively; entries 5–6 vs. 2–3, Table 2), exhibiting both comparable efficiencies at 1 mol% metal catalyst loading (entries 5–6, Table 2). Thus, both mono-metallic and bi-metallic MgAl_2O_4 -based composites displayed a better performance than the corresponding TiO_2 counterparts.

Table 2. Catalyst screening for the catalyzed hydrogenation of oleic acid using NiNP@TiO₂, CoNP@TiO₂, NiCoNP@TiO₂, NiNP@MgAl₂O₄, CoNP@MgAl₂O₄, and NiCoNP@MgAl₂O₄ composite materials ^a.

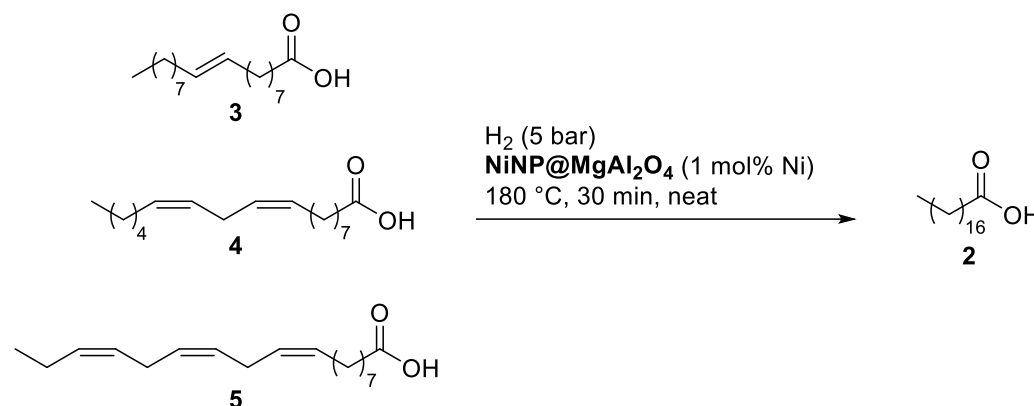
Entry	Catalyst	Metal Loading (mol%)	Conv. (%) ^b
1	CoNP@TiO ₂	1	10
2	NiNP@TiO ₂	1	65
3	NiCoNP@TiO ₂	1	31
4	CoNP@MgAl ₂ O ₄	1	12
5	NiNP@MgAl ₂ O ₄	1	96
6	NiCoNP@MgAl ₂ O ₄	1 ^c	93
7	NiCoNP@MgAl ₂ O ₄	0.6 ^d	91
8	NiNP@MgAl ₂ O ₄	0.6	35

^a Reaction conditions: 1 mmol of oleic acid (1), metal content determined by ICP-AES. ^b Determined by ¹H NMR using 4-methylanisole as internal standard; only stearic acid was observed. ^c 0.5 mol% Ni and 0.5 mol% Co. ^d 0.3 mol% Ni and 0.3 mol% Co.

Despite the lower conversions obtained for NiCoNP@TiO₂ and NiCoNP@MgAl₂O₄ in comparison to the mono-metallic nickel counterparts at 1 mol% catalyst loadings (entries 3 and 6 versus entries 2 and 5, Table 2), the poorest performance of Co could be concluded at this catalyst loading. However, it is worth mentioning that Co is permitted to operate at sub-mol% catalyst loadings with NiCoNP@MgAl₂O₄, probably hampering the deactivation of the Ni phase. Whereas the presence of oxidized nickel species such as NiO can be attributed to lower catalyst efficiency towards C=C hydrogenation of fatty acids as they usually require a preactivation step to, in situ, generate catalytically active Ni(0) species [46], cobalt oxides are well-known catalysts promoting the reduction of carboxylic acid function as well as hydrodeoxygenation of the corresponding fatty alcohols, albeit under harsher conditions (H₂ pressure and temperature) [47].

Despite the reasonably better performance of the bi-metallic composite NiCoNP@MgAl₂O₄ than NiNP@MgAl₂O₄ (entries 7–8, Table 2), we decided to pursue the reaction scope studies with the mono-metallic catalyst due to its better activity at 1 mol% Ni loading and easier characterization. It is worth mentioning that no significant loss of fatty acids by adsorption on any of the six catalytic composites was observed, recovering quantitatively the organic compounds. For further optimization parameters, see Table S3 in the Supplementary Materials.

Substrate scope studies using other mono- and poly-unsaturated C₁₈ fatty acids were then performed (Table 3). Elaidic acid, the (*E*)-isomer of oleic acid, was efficiently hydrogenated albeit in lower conversion (72% conversion; entry 1, Table 3) in comparison to oleic acid (96% conversion; entry 5, Table 3). Linoleic acid (4), showing two C=C bonds at C₉ and C₁₂, led to 69% of mono-unsaturated acid and 31% of stearic acid with nearly full conversion (entry 2, Table 3). Moreover, α-linolenic acid (5), featuring three C=C bonds at C₉, C₁₂, and C₁₅ positions, only gave 86% conversion to mono-unsaturated fatty acids (entry 3, Table 3); longer reaction time (4 h) and higher catalyst loading (2 mol% Ni) were required to completely transform both linoleic and linolenic acids to the fully saturated stearic acid (entries 4–5, Table 3). The determination of metal traces present in the organic extracts after the 4 h benchmark reaction using NiNP@MgAl₂O₄ catalyst revealed the presence of trace amounts of Ni (1.1 ppm by ICP-AES close to the detection limit of this technique), revealing negligible leaching of the catalyst and pointing to a surface reactivity of the catalyst.

Table 3. NiNP@MgAl₂O₄-catalyzed hydrogenation of unsaturated fatty acids, including industrial waste ^a.


Entry	Substrate	Conv. (%) ^b	Selectivity (%) ^b
1	3	72	100 ^c
2	4	97	70/30 ^d
3 ^e	5	86	100 ^d
4 ^f	4	>99	100 ^c
5 ^{e,f}	5	>99	100 ^c
6 ^f	Agri-food waste ^g	>99	96 ^c (4) ^h

^a Reaction conditions: 1 mmol of fatty acid, 0.01 mmol of Ni (determined by ICP-AES) unless otherwise stated.

^b Determined by ¹H NMR using 4-methylanisole as internal standard. ^c Only stearic acid was observed as a product. ^d Unsaturated fatty acids/stearic acid ratio. ^e The commercial linolenic acid used contained 20% of linoleic acid as an impurity. ^f Reaction time of 4 h using a 2 mol% Ni catalyst loading. ^g Composition of saponified raw material: 61% oleic acid, 12% linoleic acid, 3% linolenic acid, 20% stearic acid, and 4% palmitic acid. ^h Palmitic acid (4%) from the raw agri-food waste.

From an application viewpoint, we assessed the efficiency of NiNP@MgAl₂O₄ towards the valorization of fatty wastes coming from agri-food industries via selective C=C double-bond hydrogenation; the fully saturated products, namely stearic and palmitic acids and mixtures thereof are found in a large variety of products (e.g., food supplements, emulsifiers, surfactants, cosmetics, and plastics) [48]. In particular, a sample from duck fat waste supplied by the enterprise SAPOVAL was used for this study. Thus, NiNP@MgAl₂O₄ showed high efficiency in the hydrogenation of the agri-food waste, mainly constituted 76% of unsaturated fatty acids and 24% of saturated ones (stearic acid, 20%; palmitic acid, 4%). At 180 °C for 4 h using 2 mol% Ni under 5 bar H₂, the hydrogenation of the agri-food waste took place quantitatively, giving a highly enriched stearic acid sample (entry 6, Table 3).

4. Conclusions

In this contribution, a general strategy encompassing the preparation of first-row nanocomposites based on Co and Ni nanoparticles supported on MgAl₂O₄ spinel or TiO₂ and their use as sustainable catalytic materials towards selective hydrogenation processes of fatty acid substrates is reported. Thus, six original and well-defined mono-metallic (NiNP@MgAl₂O₄, CoNP@MgAl₂O₄, NiNP@TiO₂, and CoNP@TiO₂) and bi-metallic (NiCoNP@MgAl₂O₄ and NiCoNP@TiO₂) nanocomposite materials were prepared by one-step procedure following an organometallic bottom-up approach under smooth conditions, and fully characterized by (HR)TEM, ICP, PXRD, FTIR, XPS, XAS, and magnetization. The catalytic performance of MgAl₂O₄ and TiO₂-based composites towards fatty acid hydrogenation was evaluated, revealing the superior role of the former as support for the immobilization of mono- and bi-metallic Ni and Co nanoparticles, where the choice of MgAl₂O₄ support presenting both acidic and basic sites might play a better role than the amphoteric properties of TiO₂, which can induce catalyst deactivation such as the formation of Ni soaps known to block the active catalyst surface [18].

Despite their prone oxidation, XPS analysis was instrumental in assessing the content of zero-valent nickel and cobalt in the as-prepared nanocomposites. Their efficacy towards the C=C bond hydrogenation of fatty acids was evaluated. The two nickel-based systems supported on MgAl_2O_4 , namely the mono-metallic $\text{NiNP@MgAl}_2\text{O}_4$ and the bi-metallic $\text{NiNP@MgAl}_2\text{O}_4$, showed the best catalytic performances operating at 1 mol% catalyst loading and 180 °C for 30 min under 5 bar H_2 pressure. Despite the slightly lower conversion obtained for $\text{NiCoNP@MgAl}_2\text{O}_4$ in comparison to the mono-metallic $\text{NiNP@MgAl}_2\text{O}_4$ at 1 mol% catalyst loadings (93 and 96% conv., respectively), this bi-metallic composite permitted to work at sub-mol% catalyst loadings (0.6 mol%) maintaining a good conversion and exclusive selectivity towards stearic acid. $\text{NiNP@MgAl}_2\text{O}_4$ was successfully applied in the selective C=C bond hydrogenation of mono- and poly-unsaturated C_{18} fatty acids, including waste from agri-food industrial residues. Overall, the $\text{NiNP@MgAl}_2\text{O}_4$ catalyst offers great promise to carry out free fatty acid hydrogenations under milder H_2 pressures (5 bar) and shorter times (30 min to 4 h) than the literature precedents (operating up to 70 bar and 300 °C, see Table S4 in the Supplementary Materials for a selection of recent contributions).

Supplementary Materials: The following supporting information can be downloaded at: <https://www.mdpi.com/article/10.3390/nano13091435/s1>, General experimental information; Figure S1: TEM image of $\text{NiNP@MgAl}_2\text{O}_4$ (a), MgAl_2O_4 (b), and NiNP (c) after extraction with glycerol size histogram of the isolated NiNP ; Figure S2: TEM image of NiNP@TiO_2 (a), TiO_2 (b), and NiNP (c) after extraction with glycerol size histogram of the isolated NiNP ; Figure S3: TEM image of $\text{CoNP@MgAl}_2\text{O}_4$ (a), MgAl_2O_4 (b), and CoNP (c) after extraction with glycerol size histogram of the isolated CoNP ; Figure S4: TEM image of CoNP@TiO_2 (a), TiO_2 (b), and CoNP (c) after extraction with glycerol size histogram of the isolated CoNP ; Figure S5: TEM images of $\text{NiCoNP@MgAl}_2\text{O}_4$ (a), MgAl_2O_4 support after extraction of NiCoNP in glycerol (b), and glycerol phase (c); Figure S6: TEM images of NiCoNP@TiO_2 (a), TiO_2 support after extraction of NiCoNP in glycerol (b), and extracted NiCoNP (c). Size distribution (d) for extracted NiCoNP ; Figure S7: HRTEM image for NiCoNP@TiO_2 ; Figure S8: PXRD diffractogram of $\text{NiNPMgAl}_2\text{O}_4$. The (hkl) crystallographic planes correspond to MgAl_2O_4 spinel structure; Figure S9: (a) Full PXRD diffractogram of NiNP@TiO_2 . (b) Magnification of the 33–56° region. The black (hkl) crystallographic planes correspond to the anatase TiO_2 , while the blue (hkl) ones correspond to fcc nickel(0). The * symbol corresponds to rutile TiO_2 ; Figure S10: PXRD diffractogram of $\text{NiNPMgAl}_2\text{O}_4$ (left) and $\text{CoNPMgAl}_2\text{O}_4$ (right). The (hkl) crystallographic planes correspond to MgAl_2O_4 spinel structure; Figure S11: (a) Full PXRD diffractogram of CoNP@TiO_2 . (b) Magnification of the 33–56° region. The black (hkl) crystallographic planes correspond to the anatase TiO_2 , while the orange (hkl) crystallographic planes correspond to fcc cobalt (0). The * symbol corresponds to rutile TiO_2 ; Figure S12: (a) Full PXRD diffractogram of NiCoNP@TiO_2 . (b) Magnification of the 33–52° region. The black (hkl) crystallographic planes correspond to the anatase TiO_2 . The * symbol corresponds to rutile TiO_2 ; Figure S13: PXRD diffractogram of $\text{NiCoNP@MgAl}_2\text{O}_4$. The black (hkl) crystallographic planes correspond to MgAl_2O_4 spinel structure; Figure S14: Stacked DRIFT spectra of NiNP@TiO_2 (black), CoNP@TiO_2 (blue), NiCoNP@TiO_2 (green) with subtraction of TiO_2 signals and quinidine (red); Figure S15: Stacked DRIFT spectra of $\text{NiNP@MgAl}_2\text{O}_4$ (black), $\text{CoNP@MgAl}_2\text{O}_4$ (blue) and $\text{NiCoNP@MgAl}_2\text{O}_4$ (green) without subtraction of MgAl_2O_4 signals; Figure S16: Nickel $\text{L}_{2,3}$ XAS spectra of NiNP@TiO_2 (orange), $\text{NiNP@MgAl}_2\text{O}_4$ (blue), NiCoNP@TiO_2 (green), and $\text{NiCoNP@MgAl}_2\text{O}_4$ (red) with references of NiO (black), Ni(OH)_2 (black dotted line) and Ni(0) (grey); Figure S17: Cobalt $\text{L}_{2,3}$ XAS spectra of $\text{NiCoNP@MgAl}_2\text{O}_4$ (red), NiCoNP@TiO_2 (green), Co(0) reference (grey), and an atomic multiplet simulation of Co(II) (black dotted line); Figure S18: XPS analyses: Ni 2p XPS core level spectra of Ni metal, NiO and Ni(OH)_2 and corresponding envelopes from the $\text{Ni } 2p_{3/2}$ fit (left); Co 2p XPS core level spectra of Co metal, Co_3O_4 , CoO and Co(OH)_2 and corresponding envelopes from the $\text{Co } 2p_{3/2}$ fit (right); Table S1: Elemental and ICP-AES analyses; Table S2: XPS quantification (in at.%) of MgAl_2O_4 , $\text{NiNP@MgAl}_2\text{O}_4$ and $\text{NiCoNP@MgAl}_2\text{O}_4$; Table S3: Catalyst screening for the catalyzed hydrogenation of oleic acid using NiNP@TiO_2 , NiCoNP@TiO_2 , $\text{NiNP@MgAl}_2\text{O}_4$ and $\text{NiCoNP@MgAl}_2\text{O}_4$ composite materials; Table S4: Literature data on the catalyzed hydrogenation of oleic acid. References [49–52] are cited in the Supplementary Materials.

Author Contributions: Conceptualization, D.P. and M.G.; methodology, E.M., C.T. and I.F.; validation, I.F. and A.S.-M.; XPS analysis, J.-B.L. and L.M.; investigation, E.M., C.T., I.F. and A.S.-M.; data curation, E.M. and I.F.; writing—original draft preparation, D.P.; writing—review and editing, M.G.; visualization, A.S.-M.; supervision, D.P. and M.G.; project administration and funding acquisition, D.P. and M.G. All authors have read and agreed to the published version of the manuscript.

Funding: This research was funded by the POCTEFA Interreg program, grant number EFA308/19 (TRIPyr). The Centre National de la Recherche Scientifique (CNRS) and the Université Toulouse III-Paul Sabatier are gratefully acknowledged for their financial support.

Data Availability Statement: Not applicable.

Acknowledgments: We acknowledge SOLEIL for the provision of synchrotron radiation facilities at the TEMPO beamline, proposal number 20220626. The authors thank Christian Pradel for performing (HR)TEM analysis. Azzedine Bendounan and Mathieu G. Silly are acknowledged for XAS analyses and helpful discussions. The authors thank Núria Clos (Serveis Científicotècnics, Universitat de Barcelona) for performing magnetic measurements, as well as Laetitia Cavaillé and Erwan Trotoux from Sapoval for providing industrial fatty waste samples.

Conflicts of Interest: The authors declare no conflict of interest.

References

1. Sabatier, P.; Senderens, J. Action of nickel on ethylene. Ethane synthesis. *C. R. Hebd. Seances Acad. Sci.* **1897**, *124*, 1358.
2. Sabatier, P.; Senderens, J. Action of hydrogen on acetylene in presence of nickel. *C. R. Hebd. Seances Acad. Sci.* **1899**, *128*, 1173.
3. Sabatier, P. Hydrogénations et déshydrogénations par catalyse. *Ber. Dtsch. Chem. Ges.* **1911**, *44*, 1984–2001. [\[CrossRef\]](#)
4. Sabatier, P. *Catalysis in Organic Chemistry*; D. Van Nostrand Company: New York, NY, USA, 1922.
5. Fouilloux, P. The nature of raney nickel, its adsorbed hydrogen and its catalytic activity for hydrogenation reactions (review). *Appl. Catal.* **1983**, *8*, 1–42. [\[CrossRef\]](#)
6. Murray, R. Method of Producing Finely-Divided Nickel. U.S. Patent US1628190A, 10 May 1927.
7. Murray, R. Method of Preparing Catalytic Material. U.S. Patent US1915473A, 27 June 1933.
8. Aller, B. Raney cobalt hydrogenation catalysts. I. The preparation of the catalyst. *J. Appl. Chem.* **1957**, *7*, 130–134. [\[CrossRef\]](#)
9. Heinz, I.; Gerhard, M. Process for the Production of Hexamethylene Diamine. U.S. Patent US3048635A, 7 August 1962.
10. Gray, J.I.; Russell, L.F. Hydrogenation catalysts—Their effect on selectivity. *J. Am. Oil Chem. Soc.* **1979**, *56*, 36–44. [\[CrossRef\]](#)
11. Devred, F.; Reinhart, G.; Iles, G.N.; van der Klugt, B.; Adkins, N.J.; Bakker, J.W.; Nieuwenhuys, B.E. Synchrotron X-ray microtomography of Raney-type nickel catalysts prepared by gas atomisation: Effect of microstructure on catalytic performance. *Catal. Today* **2011**, *163*, 13–19. [\[CrossRef\]](#)
12. Hata, K.; Motoyama, I.; Sakai, K. The Urushibara hydrogenation catalysts: A review. *Org. Prep. Proced. Int.* **1972**, *4*, 179–209. [\[CrossRef\]](#)
13. Genchi, G.; Carocci, A.; Lauria, G.; Sinicropi, M.S.; Catalano, A. Nickel: Human Health and Environmental Toxicology. *Int. J. Environ. Res. Public Health* **2020**, *17*, 679. [\[CrossRef\]](#) [\[PubMed\]](#)
14. Yang, P.; Zhang, L.J.; Wang, X.J.; Wang, Z.L. Exploring the management of industrial hazardous waste based on recent accidents. *J. Loss Prev. Process Ind.* **2020**, *67*, 104224. [\[CrossRef\]](#)
15. Leyssens, L.; Vinck, B.; Van Der Straeten, C.; Wuyts, F.; Maes, L. Cobalt toxicity in humans—A review of the potential sources and systemic health effects. *Toxicology* **2017**, *387*, 43–56. [\[CrossRef\]](#) [\[PubMed\]](#)
16. Unice, K.M.; Monnot, A.D.; Gaffney, S.H.; Tvermoes, B.E.; Thuett, K.A.; Paustenbach, D.J.; Finley, B.L. Inorganic cobalt supplementation: Prediction of cobalt levels in whole blood and urine using a biokinetic model. *Food Chem. Toxicol.* **2012**, *50*, 2456–2461. [\[CrossRef\]](#)
17. Tvermoes, B.E.; Paustenbach, D.J.; Kerger, B.D.; Finley, B.L.; Unice, K.M. Review of cobalt toxicokinetics following oral dosing: Implications for health risk assessments and metal-on-metal hip implant patients. *Crit. Rev. Toxicol.* **2015**, *45*, 367–387. [\[CrossRef\]](#)
18. Anneken, D.J.; Both, S.; Christoph, R.; Fieg, G.; Steinberger, U.; Westfechtel, A. Fatty Acids. In *Ullmann's Encyclopedia of Industrial Chemistry*; Verlag Chemie: Hoboken, NJ, USA, 2006. [\[CrossRef\]](#)
19. Taylor, N.J.; Pottebaum, A.J.; Uz, V.; Laine, R.M. The bottom up approach is not always the best processing method: Dense α - Al_2O_3 / NiAl_2O_4 composites. *Adv. Funct. Mater.* **2014**, *24*, 3392–3398. [\[CrossRef\]](#)
20. Ribeiro, N.F.P.; Neto, R.C.R.; Moya, S.F.; Souza, M.M.V.M.; Schmal, M. Synthesis of NiAl_2O_4 with high surface area as precursor of Ni nanoparticles for hydrogen production. *Int. J. Hydrog. Energy* **2010**, *35*, 11725–11732. [\[CrossRef\]](#)
21. Sahli, N.; Petit, C.; Roger, A.C.; Kiennemann, A.; Libs, S.; Bettahar, M.M. Ni catalysts from NiAl_2O_4 spinel for CO_2 reforming of methane. *Catal. Today* **2006**, *113*, 187–193. [\[CrossRef\]](#)
22. Zhang, X.; Lu, G.; Hoffmann, M.J.; Metselaar, R. Properties and interface structures of Ni and Ni-Ti alloy toughened Al_2O_3 ceramic composites. *J. Eur. Ceram. Soc.* **1995**, *15*, 225–232. [\[CrossRef\]](#)
23. Breval, E.; Deng, Z.; Chiou, S.; Pantano, C.G. Sol-gel prepared Ni-alumina composite materials. *J. Mater. Sci.* **1992**, *27*, 1464–1468. [\[CrossRef\]](#)

24. Itzhak, H.; Danut, D.; Ersan, Ü.; Alan, F.Y.; Elizabeth, H.A.; Jingzhu, H.; Maddury, S.S. The effect of pressure on the structure of NiAl_2O_4 . *J. Phys. Condens. Matter* **2002**, *14*, 10511. [\[CrossRef\]](#)
25. Barroso, M.N.; Galetti, A.E.; Abello, M.C. Ni catalysts supported over MgAl_2O_4 modified with Pr for hydrogen production from ethanol steam reforming. *Appl. Catal. A Gen.* **2011**, *394*, 124–131. [\[CrossRef\]](#)
26. Yu, S.; Hu, Y.; Cui, H.; Cheng, Z.; Zhou, Z. Ni-based catalysts supported on MgAl_2O_4 with different properties for combined steam and CO_2 reforming of methane. *Chem. Eng. Sci.* **2021**, *232*, 116379. [\[CrossRef\]](#)
27. Ganesh, I. A review on magnesium aluminate (MgAl_2O_4) spinel: Synthesis, processing and applications. *Int. Mater. Rev.* **2013**, *58*, 63–112. [\[CrossRef\]](#)
28. Sinhamahapatra, S.; Das, P.; Dana, K.; Tripathi, H.S. Magnesium Aluminate Spinel: Structure, Properties, Synthesis and Applications. *Trans. Indian Ceram. Soc.* **2022**, *81*, 97–120. [\[CrossRef\]](#)
29. Sági, A.; Rajkumar, T.; Kiss, J.; Kukovecz, Á.; Kónya, Z.; Somorjai, G.A. Metallic Nanoparticles in Heterogeneous Catalysis. *Catal. Lett.* **2021**, *151*, 2153–2175. [\[CrossRef\]](#)
30. Reina, A.; Favier, I.; Pradel, C.; Gómez, M. Stable Zero-Valent Nickel Nanoparticles in Glycerol. *Adv. Synth. Catal.* **2018**, *360*, 3544–3552. [\[CrossRef\]](#)
31. Pérez Alonso, A.; Mauriés, S.; Ledeuil, J.-B.; Madec, L.; Pham Minh, D.; Pla, D.; Gómez, M. Nickel Nanoparticles Immobilized on Pristine Halloysite: An Outstanding Catalyst for Hydrogenation Processes. *ChemCatChem* **2022**, *14*, e2022007. [\[CrossRef\]](#)
32. Favier, I.; Pla, D.; Gómez, M. Palladium nanoparticles in polyols: Synthesis, catalytic couplings and hydrogenations. *Chem. Rev.* **2020**, *120*, 1146–1183. [\[CrossRef\]](#)
33. Garg, G.; Foltran, S.; Favier, I.; Pla, D.; Medina-González, Y.; Gómez, M. Palladium Nanoparticles Stabilized by Novel Choline-based Ionic Liquids in Glycerol Applied in Hydrogenation Reactions. *Catal. Today* **2020**, *346*, 69–75. [\[CrossRef\]](#)
34. Mamontova, E.; Favier, I.; Pla, D.; Gómez, M. Chapter Two—Organometallic interactions between metal nanoparticles and carbon-based molecules: A surface reactivity rationale. In *Advances in Organometallic Chemistry*; Pérez, P.J., Ed.; Academic Press: Cambridge, MA, USA, 2022; Volume 77, pp. 43–103. [\[CrossRef\]](#)
35. Leal-Duaso, A.; Favier, I.; Pla, D.; Pires, E.; Gómez, M. Design of Glycerol-Based Solvents for the Immobilization of Palladium Nanocatalysts: A Hydrogenation Study. *ACS Sustain. Chem. Eng.* **2021**, *9*, 6875–6885. [\[CrossRef\]](#)
36. Billas, I.M.L.; Châtelain, A.; de Heer, W.A. Magnetism from the Atom to the Bulk in Iron, Cobalt, and Nickel Clusters. *Science* **1994**, *265*, 1682–1684. [\[CrossRef\]](#) [\[PubMed\]](#)
37. Ishizaki, T.; Yatsugi, K.; Akedo, K. Effect of Particle Size on the Magnetic Properties of Ni Nanoparticles Synthesized with Trioctylphosphine as the Capping Agent. *Nanomaterials* **2016**, *6*, 172. [\[CrossRef\]](#) [\[PubMed\]](#)
38. Nishikawa, M.; Kita, E.; Erata, T.; Tasaki, A. Enhanced magnetization in cobalt/magnesium oxide multilayer thin films. *J. Magn. Magn. Mater.* **1993**, *126*, 303. [\[CrossRef\]](#)
39. Lozhkomoev, A.S.; Pervikov, A.V.; Kazantsev, S.O.; Suliz, K.V.; Veselovskiy, R.V.; Miller, A.A.; Lerner, M.I. Controlled Oxidation of Cobalt Nanoparticles to Obtain Co/CoO/Co₃O₄ Composites with Different Co Content. *Nanomaterials* **2022**, *12*, 2523. [\[CrossRef\]](#) [\[PubMed\]](#)
40. Guo, B.; Xu, Y.; Zhou, S. Morphology dependence of low temperatures exchange bias Co/CoO core-shell nanoparticles/spheres by eco-friendly solvothermal route. *AIP Adv.* **2018**, *8*, 115115. [\[CrossRef\]](#)
41. Xie, X.; Ni, C.; Lin, Z.; Wu, D.; Sun, X.; Zhang, Y.; Wang, B.; Du, W. Phase and morphology evolution of high dielectric CoO/Co₃O₄ particles with Co₃O₄ nanoneedles on surface for excellent microwave absorption application. *Chem. Eng. J.* **2020**, *396*, 125205. [\[CrossRef\]](#)
42. Srivastava, A.K.; Madhavi, S.; Menon, M.; Ramanujan, R.V. Synthesis of Co/Co₃O₄ Nanocomposite Particles Relevant to Magnetic Field Processing. *J. Nanosci. Nanotechnol.* **2010**, *10*, 6580–6585. [\[CrossRef\]](#)
43. Van Schooneveld, M.M.; Kurian, R.; Juhin, A.; Zhou, K.; Schlappa, J.; Strocov, V.N.; Schmitt, T.; de Groot, F.M.F. Electronic Structure of CoO Nanocrystals and a Single Crystal Probed by Resonant X-ray Emission Spectroscopy. *J. Phys. Chem. C* **2012**, *116*, 15218–15230. [\[CrossRef\]](#)
44. Belyakov, A.V.; Faikov, P.P.; Tsvigunov, A.N.; Andrianov, N.T.; Ivleva, Y.V. Synthesis of aluminomagnesian spinel with excess magnesium oxide under varying flow rates of cation mass transfer. *Glass Ceram.* **2006**, *63*, 46–51. [\[CrossRef\]](#)
45. Varga, E.; Pusztai, P.; Óvári, L.; Oszkó, A.; Erdőhelyi, A.; Papp, C.; Steinrück, H.P.; Kónya, Z.; Kiss, J. Probing the interaction of Rh, Co and bimetallic Rh–Co nanoparticles with the CeO₂ support: Catalytic materials for alternative energy generation. *Phys. Chem. Chem. Phys.* **2015**, *17*, 27154–27166. [\[CrossRef\]](#)
46. Song, S.; Yao, S.; Cao, J.; Di, L.; Wu, G.; Guan, N.; Li, L. Heterostructured Ni/NiO composite as a robust catalyst for the hydrogenation of levulinic acid to γ -valerolactone. *Appl. Catal. B* **2017**, *217*, 115–124. [\[CrossRef\]](#)
47. Jia, W.; Xu, G.; Liu, X.; Zhou, F.; Ma, H.; Zhang, Y.; Fu, Y. Direct Selective Hydrogenation of Fatty Acids and Jatropa Oil to Fatty Alcohols over Cobalt-Based Catalysts in Water. *Energy Fuels* **2018**, *32*, 8438–8446. [\[CrossRef\]](#)
48. Van Rooijen, M.A.; Mensink, R.P. Palmitic Acid Versus Stearic Acid: Effects of Interesterification and Intakes on Cardiometabolic Risk Markers—A Systematic Review. *Nutrients* **2020**, *12*, 615. [\[CrossRef\]](#) [\[PubMed\]](#)
49. Biesinger, M.C.; Payne, B.P.; Lau, L.W.M.; Gerson, A.; Smart, R.S.C. X-ray photoelectron spectroscopic chemical state quantification of mixed nickel metal, oxide and hydroxide systems. *Surf. Interface Anal.* **2009**, *41*, 324–332. [\[CrossRef\]](#)
50. Biesinger, M.C.; Lau, L.W.; Gerson, A.R.; Smart, R.S.C. The role of the Auger parameter in XPS studies of nickel metal, halides and oxides. *Phys. Chem. Chem. Phys.* **2012**, *14*, 2434–2442. [\[CrossRef\]](#) [\[PubMed\]](#)

51. Biesinger, M.C.; Payne, B.P.; Grosvenor, A.P.; Lau, L.W.M.; Gerson, A.R.; Smart, R.S.C. Resolving surface chemical states in XPS analysis of first row transition metals, oxides and hydroxides: Cr, Mn, Fe, Co and Ni. *Appl. Surf. Sci.* **2011**, *257*, 2717–2730. [[CrossRef](#)]
52. Polack, F.; Silly, M.; Chauvet, C.; Lagarde, B.; Bergeard, N.; Izquierdo, M.; Chubar, O.; Krizmancic, D.; Ribbens, M.; Duval, J.P.; et al. TEMPO: A New Insertion Device Beamline at SOLEIL for Time Resolved Photoelectron Spectroscopy Experiments on Solids and Interfaces. *AIP Conf. Proc.* **2010**, *1234*, 185–188. [[CrossRef](#)]

Disclaimer/Publisher’s Note: The statements, opinions and data contained in all publications are solely those of the individual author(s) and contributor(s) and not of MDPI and/or the editor(s). MDPI and/or the editor(s) disclaim responsibility for any injury to people or property resulting from any ideas, methods, instructions or products referred to in the content.